Timepix3 semiconductor pixel detector as runaway electron diagnostics at the GOLEM tokamak

Štěpán Malec[1], **M. Tunkl**[1,2], **L. Lobko**[1,2], **O. Ficker**[1,2], **J. Čeřovský**[1,2], **V. Svoboda**[1], **G. I. Pokol**[1,4]

[1]Faculty of Nuclear Sciences and Physical Engineering CTU in Prague, Czech Republic
[2]Department of Applied Physics, Ghent University, 9000 Ghent, Belgium
[3]Institute of Plasma Physics of the CAS, Prague, Czech Republic
[4]Department of Nuclear Techniques, Faculty of Natural Sciences, Budapest University of Technology and Economics, Budapest, Hungary

E-mail: `malecste@cvut.cz`

December 2025

Abstract. The Timepix3 semiconductor pixel detector was investigated as a diagnostic tool for runaway electron (RE) related hard X-ray (HXR) emission at the GOLEM tokamak. We combined high-resolution spatial, temporal and energy measurements from the AdvaPix Timepix3 detector with time-frequency analysis of magnetic signals (Mirnov coils) to explore correlations between HXR bursts and MHD activity. Continuous Wavelet Transform (CWT) based ridge extraction and minimum-coherence measures were used to identify common oscillatory components and to compute phase shifts between HXR signals and Mirnov coils signals. We observe statistically significant coherence between the Timepix3 HXR time series and Mirnov coil signals in distinct time–frequency bands, and find a systematic phase shift in the majority studied discharges, suggesting modulation of RE losses by MHD modes.

The strongest HXR bursts appear to coincide with periods of stronger MHD activity. These results demonstrate that the Timepix3 detector, combined with time–frequency coherence analysis, is a promising tool for studying the interplay between MHD modes and runaway electron dynamics.

Keywords: Timepix3, runaway electrons, GOLEM, tokamak, Mirnov coils, wavelet analysis

1. Introduction

During a tokamak plasma discharge, a fraction of electrons can be accelerated to relativistic energies. These particles, referred to as runaway electrons (REs), can enter the runaway regime, for example, through the Dreicer mechanism [1]. High-energy REs can either interact with the plasma or, if insufficiently confined by the magnetic field, escape and strike tokamak components. Such interactions can be harmful to the device [2, 3]. Since the mechanisms of RE generation and transport are not yet fully understood, the development of diagnostics is essential to provide key information on the temporal evolution, trajectories, and impact locations of RE populations on plasma-facing components. Characterization of runaway electrons (RE) using hard X-ray (HXR) detection is an important tool for understanding their generation.

Scintillation detectors are a widely used group of HXR detectors in tokamaks. Among the most commonly used scintillation materials is NaI(Tl), which has been installed as the basic HXR diagnostics in many tokamaks, including JET [4], COMPASS [5, 6, 7, 8], WT-3 [9], TUMAN-3M [10], J-TEXT [11],HL-2 [12] and HT-7 [13, 14]. Furthermore, the scintillator LaBr3(Ce) has been deployed on JET [4], TCV [15], ASDEX Upgrade [16, 17], TUMAN-3M [18] and FT-2 [18, 19], while BGO detectors have been used on JET [4], TORE SUPRA [20], FT-2 [18] and EAST [21]. Other scintillation materials have also been employed, including ZnS(Ag) [8, 5] or CsI(Tl) for HXR cameras at JET [4].

Another diverse group of HXR detectors consists of semiconductor detectors, most often based on CdTe sensors, which have been implemented on HT-7 [13, 14], HL-2 [22] and EAST [21]. Detectors with CdTe sensors are also used in HXR camera systems installed on machines including TORE SUPRA [23], TCV [24], COMPASS [7] and HL-2 [12], and can form part of HXR tomography, as demonstrated on TORE SUPRA [25, 23] and TCV [24]. Semiconductor detectors are mainly designed for detecting radiation with energies up to hundreds of keV, primarily due to their smaller detection volume compared to scintillation crystals. In contrast, the scintillation detectors used can effectively detect radiation with energies of several MeV; however, pile-up effects and saturation can represent a limitation. Another semiconductor material used for HXR cameras is CdZnTe, with camera systems comprising dozens of detectors reported in [26, 27].

Currently, standard HXR diagnostics on the GOLEM tokamak consist of two 1” × 1” CeBr3 scintillators, one 2” × 2” NaI(Tl) scintillator, and one 1” × 1” YAP(Ce) scintillator. Details about HXR diagnostics can be found in [28].

A silicon strip detector with 32 strips was also tested on the GOLEM tokamak. Works presented in [29] and [30] describe the use of semiconductor strip detectors for direct RE measurements. The dimensions of each strip are 250 µm × 18 mm and the sensor thickness is 525 µm [29, 30]. The use of semiconductor pixel detector MediPix2 with 300 µm thick sensor for indirect RE measurements via HXR is described in work [29].

A semiconductor pixel detector Timepix3 [31] has previously been employed on the GOLEM tokamak, for example, see [32], [33] and [34]. The Timepix3 detector has also been used on the COMPASS tokamak [34]. This work describes the capabilities of the Timepix3 detector on the GOLEM tokamak and demonstrates its suitability for studying correlations between HXR signals and magnetic activity detected using Mirnov coils. An analysis of the coherence between these signals enables the identification of phenomena that are difficult to resolve using individual diagnostics alone. The observed correlations imply that runaway electrons of different energies may interact with different MHD modes.

Coherence analysis between diagnostic signals using wavelet methods was successfully applied in [39] for CASTOR tokamak discharges and in [40, 41] for the investigation of modes at ASDEX Upgrade. Frequency analysis of Timepix3 signals and their correlations with magnetic data on the COMPASS tokamak were addressed in [34]. Frequency analysis is also used to investigate RE transport and magnetic perturbations in COMPASS tokamak [5, 42] and IR-T1 [43].

This paper is organized as follows. Section 2 first introduces the tokamak GOLEM, followed by a description of the AdvaPix Timepix3 detection module, and concludes with an overview of the experimental setup. Section 3 then presents the procedure used to process signals from the Timepix3 detector and magnetic diagnostics. Individual diagnostic signals are analysed using a continuous wavelet transform (CWT), while the wavelet minimum coherence (WMC) method is employed to quantify the coherence between them. To assess whether HXR emission is modulated by MHD modes at specific frequencies, coherence ridges are identified and the phase shift between MHD and HXR signals is calculated along these ridges. The results obtained from this analysis are summarized at the end of this section.

2. Setup and Diagnostics

This section describes the experimental setup and diagnostics. First, the GOLEM tokamak and its main parameters are summarized, then the AdvaPix Timepix3 detector is presented, followed by details on detector placement, the Be window, limiter Mirnov coils, and data acquisition. Representative spectroscopic results demonstrating detector performance are included.

2.1. The GOLEM Tokamak

The GOLEM tokamak, located at the Faculty of Nuclear Sciences and Physical Engineering of the Czech Technical University in Prague, is the oldest still-operating tokamak. It is primarily used for educational purposes and can be remotely controlled via a web interface [35]. Among the main advantages of the GOLEM tokamak are its high discharge reproducibility and high repetition rate. During experimental campaigns, the device can be easily modified, allowing adjustments or relocation of diagnostics, provided that the diagnostics themselves permit such modifications, between discharges. Owing to this flexibility, the GOLEM tokamak provides an excellent experimental environment for testing and developing new diagnostics, including those dedicated to runaway-electron studies.

The GOLEM tokamak has an iron transformer core, a molybdenum limiter and a circular cross-section vacuum chamber. The toroidal field is generated by 28 copper coils. The main parameters are summarised in Table 1.

Major radius	$R_0 = 0.4$ m
Chamber minor radius	$r_0 = 0.1$ m
Limiter radius	$a = 0.085$ m
Toroidal magnetic field	$B_t < 0.8$ T
Plasma current	$I_p < 14$ kA
Discharge duration	$\tau < 50$ ms
Plasma density	$n_e(0) \approx 0.5 - 3 \times 10^{19}$ m^{-3}
Plasma temperature	$T_e(0) \leq 100$ eV

Table 1: Main parameters of the GOLEM tokamak. [36]

2.2. AdvaPix Timepix3 Detector

The AdvaPix Timepix3 detection module, shown in Figure 1, is a semiconductor pixel detector intended for the detection of ionizing radiation. The detection modules are equipped with a sensor, either CdTe or Si, divided into 256 × 256 pixels. Each pixel represents one separate detector (spectrometer) with a size of 55 × 55 µm with a time resolution of up to 1.5625 ns and a maximum reading speed of up to 40 million pixels per 1 second [37]. Timepix3 [31] is a universal integrated circuit suitable for readout ?signals? semiconductor solid-state pixelated sensors and gaseous detectors [31]. The chip is designed and manufactured in 130 nm CMOS technology.

A schematic illustration of the event readout from the sensor is shown in Figure 2. The signal generated by the passage of a photon or a charged particle is amplified in each pixel and compared with a predefined threshold level by a comparator. Exceeding the threshold triggers the registration of an event and activates the measurement of the time of arrival (ToA) and the time over threshold (ToT). The ToA value is determined with the accuracy of the clock signal, while the ToT provides information proportional to the collected charge, and thus to the particle's energy. Each pixel is equipped with its own counting circuit that stores these data, and the resulting information is subsequently read out from the pixel matrix into the control electronics.

2.3. Experimental setup

The Timepix3 detector with a 1 mm thick silicon sensor was installed in the equatorial plane of the tokamak, with a line of sight into the plasma through a beryllium window. This window significantly reduces the attenuation of HXR near the detector energy threshold compared to the tokamak wall. A schematic representation of the experimental arrangement of the detector and limiter Mirnov coils is shown in Figure 3. All diagnostics on the GOLEM tokamak are triggered by a common trigger signal, ensuring synchronization between the diagnostics. The arrangement of the Mirnov coils is shown

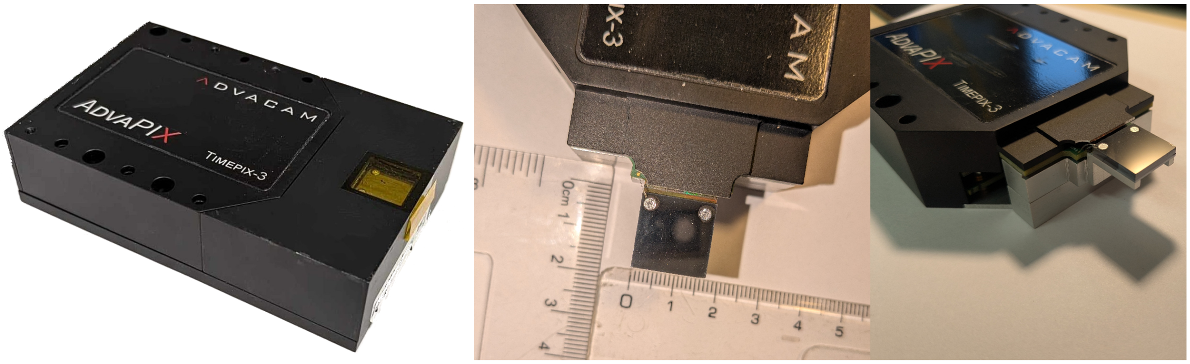

Figure 1: The first photo shows the AdvaPix Timepix3 detection module. The second and third photos show the sensor in detail with a scale.

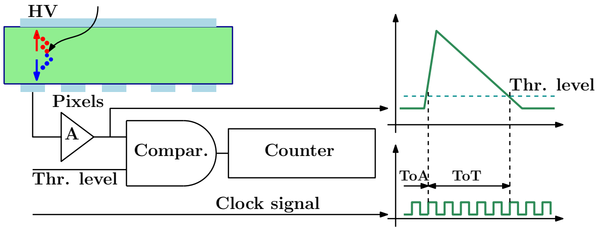

Figure 2: Schematic representation of sensor event readout.

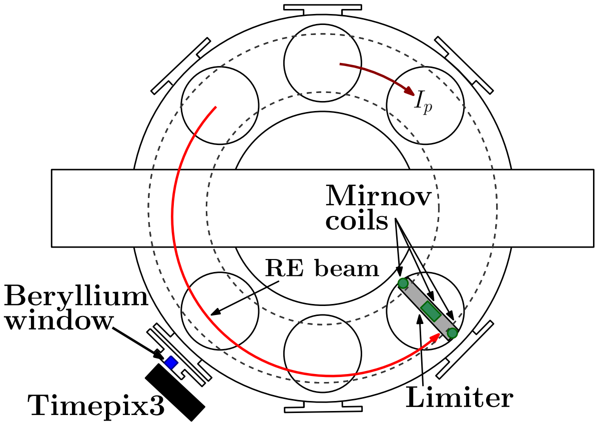

Figure 3: Schematic illustration of the placement of the AdvaPix Timepix3 detection module with a line of sight through the beryllium window and the location of the limiter Mirnov coils. The directions of the plasma current and runaway electrons are also indicated.

in Figure 4.

The Timepix3 detector was temperature-stabilized at 20 °C, which is the same temperature at which the detector calibration was performed. The spectroscopic performance of the detector is demonstrated by measuring the spectrum of a known ionizing radiation source, ^{241}Am. This spectrum is shown in Figure 5. The spectrum shows a peak with an energy of 59.54 keV and a hint of a lower peak at 26.34 keV.

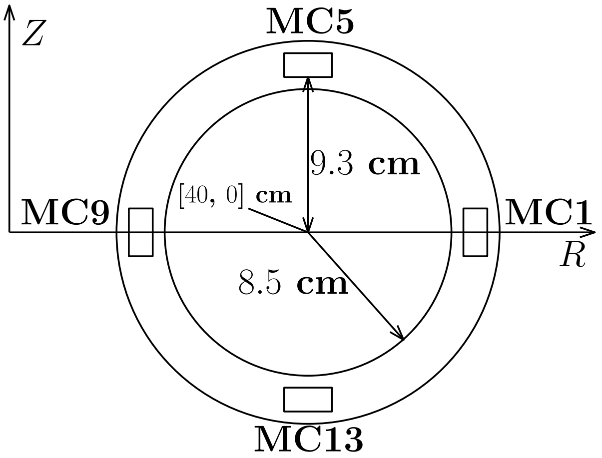

Figure 4: Schematic illustration of the arrangement of the individual Mirnov coils on the GOLEM tokamak.

This corresponds to the characteristic gamma radiation of ^{241}Am, or, more precisely, of ^{237}Np, which is produced as a decay product of ^{241}Am. The range 13.759 keV – 20.784 keV corresponds to the characteristic X-ray radiation for the L lines of ^{237}Np. The values of individual energies of characteristic radiation are taken from [38]. Since the detection efficiency of this sensor decreases exponentially from approximately 15 keV, a relatively large number of low-energy photons are detected. At the beginning of the measured spectrum (5 keV), there is a threshold, and the measured interactions may not have a physical basis. The spectra differ slightly when the sensor is irradiated from the front (top side of the sensor) and from the back (side of the sensor with readout electrodes). This may be caused by charge diffusion during its collection on the readout electrodes. This demonstration of measuring a known source of ionizing radiation shows the detector's ability to perform measurements with energy resolution and confirms the correct calibration of the detector.

3. Analysis of HXR signals and associated MHD activity

This section presents an analysis of hard X-ray (HXR) signals measured by the Timepix3 detector during plasma discharges in the GOLEM tokamak and their relation to magnetohydrodynamic (MHD) activity. First, the basic characteristics of the detected HXR signals are discussed, including their temporal evolution, spatial distribution on the detector, and energy spectra. Next, a time-frequency analysis based on continuous wavelet transforms is used to investigate the correlation between HXR emissions and magnetic fluctuations measured by Mirnov coils. Wavelet coherence and ridge analysis are then employed to identify time-localized, frequency-dependent correlations, as well as to examine the phase relationships between diagnostics. This provides insight into the potential modulation of runaway electron losses by MHD modes.

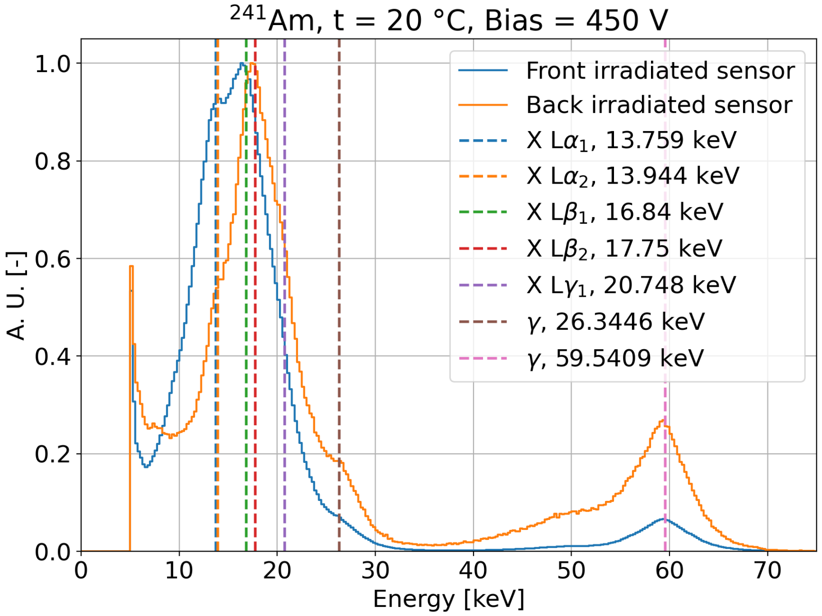

Figure 5: Spectrum of ^{241}Am when irradiating the sensor from the top and from the back (from the side of the readout electrodes). The spectra are normalized to the peak relative to Lβ.

3.1. Characteristics of the HXR time signals

In Figure 6, the overall hit map of detector pixels of the Timepix3 detector for the representative discharge #46422 [51] is shown. This hit map shows how many times a given detector sensor pixel was above the energy threshold during the discharge. For further analysis, however, it is necessary to merge the corresponding pixels into clusters [31]. The Timepix3 detector provides excellent spatial, energy, and time resolution, enabling the study of individual interactions. Interaction clustering is performed with a time resolution of 50 ns. The detector was placed at the beryllium window, and part of the sensor has a direct line of sight through the beryllium window into the tokamak. In Figure 6, two circles are shown that delineate the areas of the sensor with direct line of sight through the beryllium window and the rest of the sensor. The annulus between the red and green circles is not included in the analyses (unless stated otherwise), since the boundary of the beginning of the beryllium window is not entirely clear.

In Figure 7, the first two plots show the main parameters of the Golem tokamak, followed by the time evolution of the number of detected interactions during the discharge. The discharge is divided here into three time regions with the same number of interactions detected in each window. The energy spectra from the individual parts of the discharge are shown in Figure 8. A detail of the detector sensor during a short discharge segment, in which the highest-energy photons were detected, is shown in Figure 9. In the next two plots of Figure 7, the time evolution of the number of interactions and their energies from the sensor area with line of sight through the

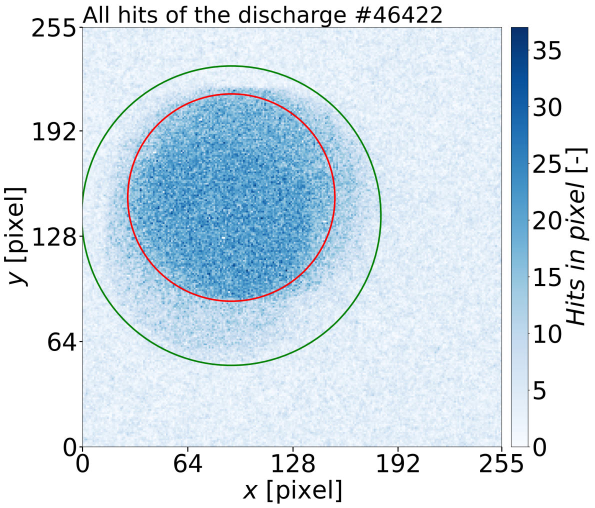

Figure 6: The overall hit map of detector pixels of the Timepix3 detector for the representative discharge #46422. The hit map is divided into two main areas - inside red circle and outside green circle.

beryllium window and from the rest of the detector are shown.

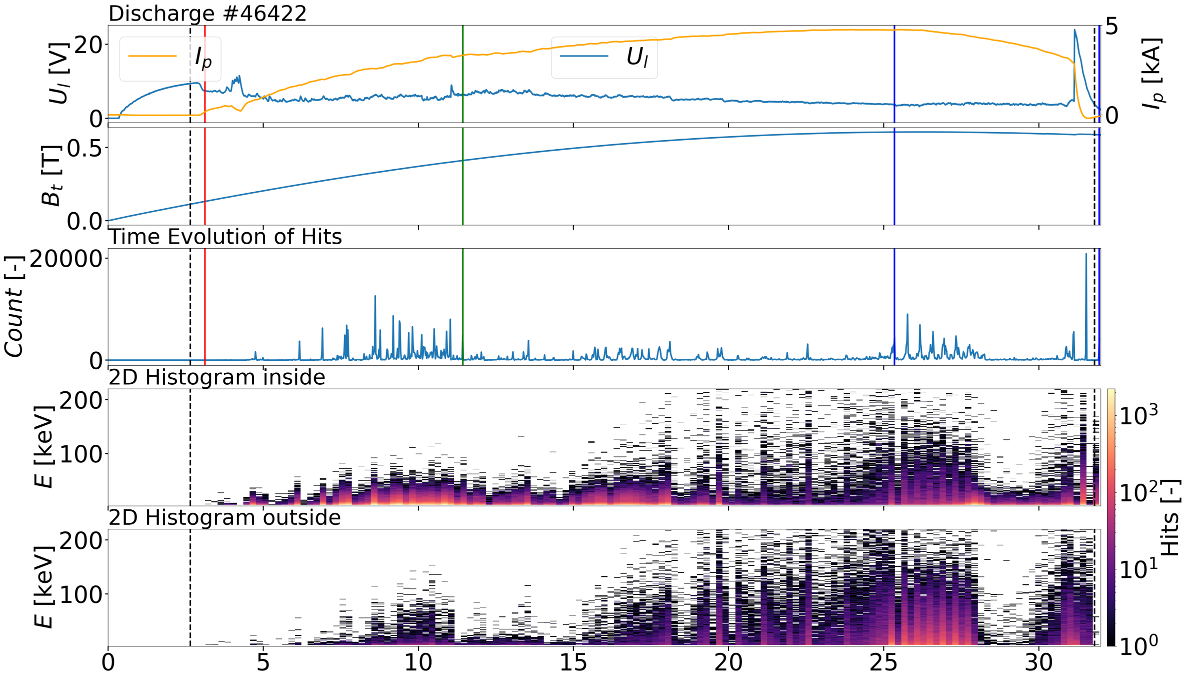

Figure 7: The top two lines of the figure show the main GOLEM tokamak parameters. The next line shows the time evolution of the interactions detected by the Timepix3 detector. The discharge is divided into three intervals with equal interaction counts. Lines 4 and 5 show the time evolution and energy distributions by spatial separation.

For each time interval, as shown in the third panel of Figure 7, the energy spectrum of the entire sensor is presented. Figure 8 shows the sensor hit maps for each interval along with the corresponding energy spectra. It is evident that RE losses reach the highest energies in the central interval.

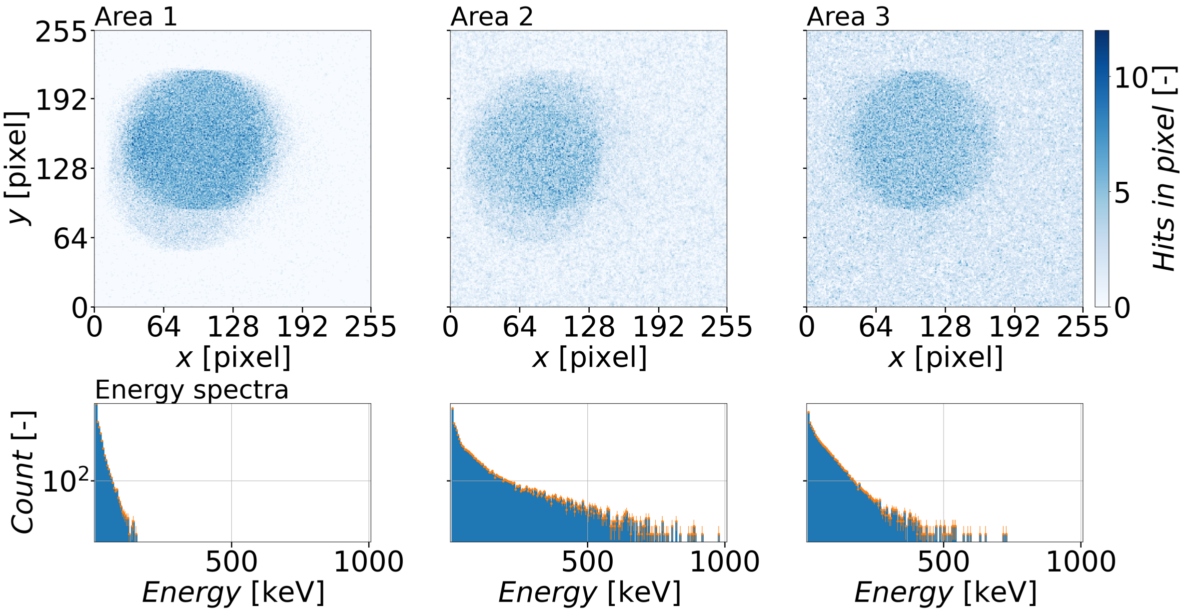

Figure 8: Comparison of the individual time intervals. Interval 2 contains the most energetic interactions (for instance, see Figure 9).

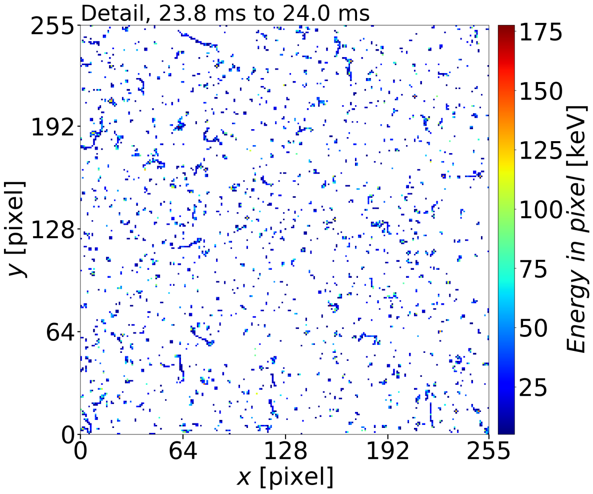

Figure 9: Sensor display over a short segment of the discharge, showing tracks of individual interactions.

3.2. Time–frequency wavelet analysis and coherence of MHD activity and HXR signals

This work employs time–frequency analysis to identify MHD-related modulations of HXR signals. Because the standard Fourier transform loses temporal information and the short-time Fourier transform (STFT) requires a fixed window with constant time–frequency resolution (thus forcing a trade-off between time and frequency localisation), we use the continuous wavelet transform (CWT) [44], which provides adaptive time–frequency localisation suitable for the short transient events observed in GOLEM discharges. In tokamak diagnostics, wavelet methods (typically using Morlet-like analytic wavelets) have been used to analyse Mirnov, soft X-ray and other signals for mode identification and for studying correlations between magnetohydrodynamics activity and radiation diagnostics [39, 45].

For signal $x(t) \in L^2(\mathbb{R})$ and mother wavelet $\psi(t)$, the CWT is defined as

$$W(\mu, \xi) = \int_{-\infty}^{\infty} x(t) \, \frac{1}{\sqrt{|\mu|}} \, \psi^* \left(\frac{t - \xi}{\mu} \right) \, dt, \qquad (1)$$

where μ denotes the scale, ξ the time shift and the * denotes complex conjugation. Small scales μ correspond to high pseudo-frequencies and vice versa; further properties and practical aspects of the CWT are discussed in the literature [46, 47, 48].

Raw signals from the limiter Mirnov coils are displayed in Figure 10. In Figure 11 are the energy density distributions and in Figure 12 are the smoothed energy density distributions of the continuous wavelet transform $(\overline{W_x(\mu, \xi)^2})$ of HXR signals from the Timepix3 detector and the signals from the Mirnov coils.

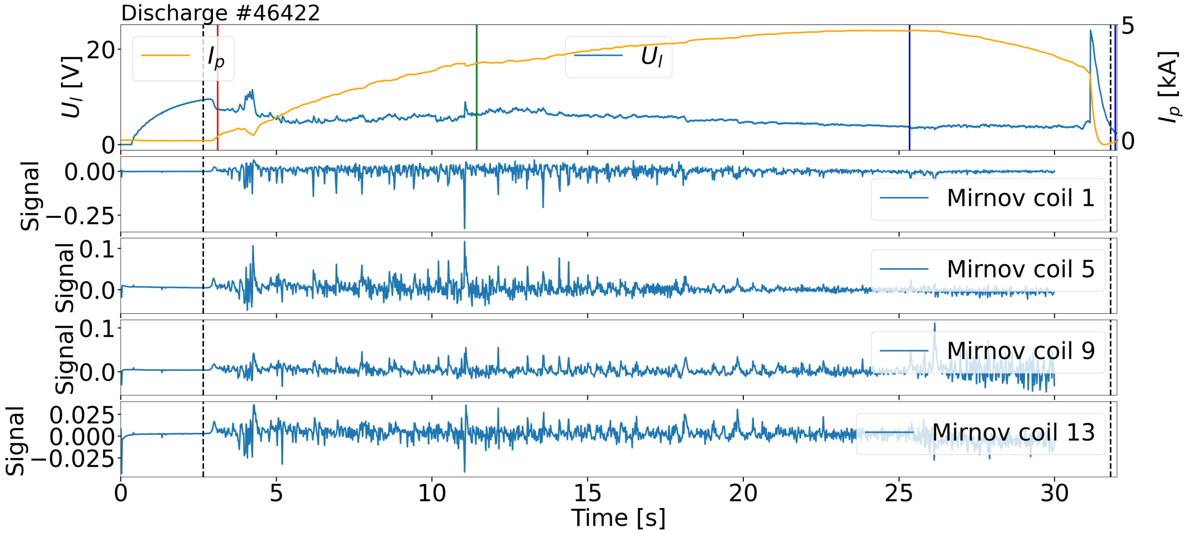

Figure 10: The top line of the figure show the U_{loop} and plasma current during plasma discharge of the GOLEM tokamak. The next four lines show raw signals of Mirnov coils.

Each signal was analyzed using the continuous wavelet transform with the analytic Morlet wavelet of order 3. This choice was motivated by the nature of discharges in the GOLEM tokamak, where rapid transient events occur and good temporal resolution is therefore required. The use of a third-order Morlet wavelet represents a compromise between time and frequency resolution. Lower-order Morlet wavelets provide better localization of short-lived features in time but at the expense of frequency

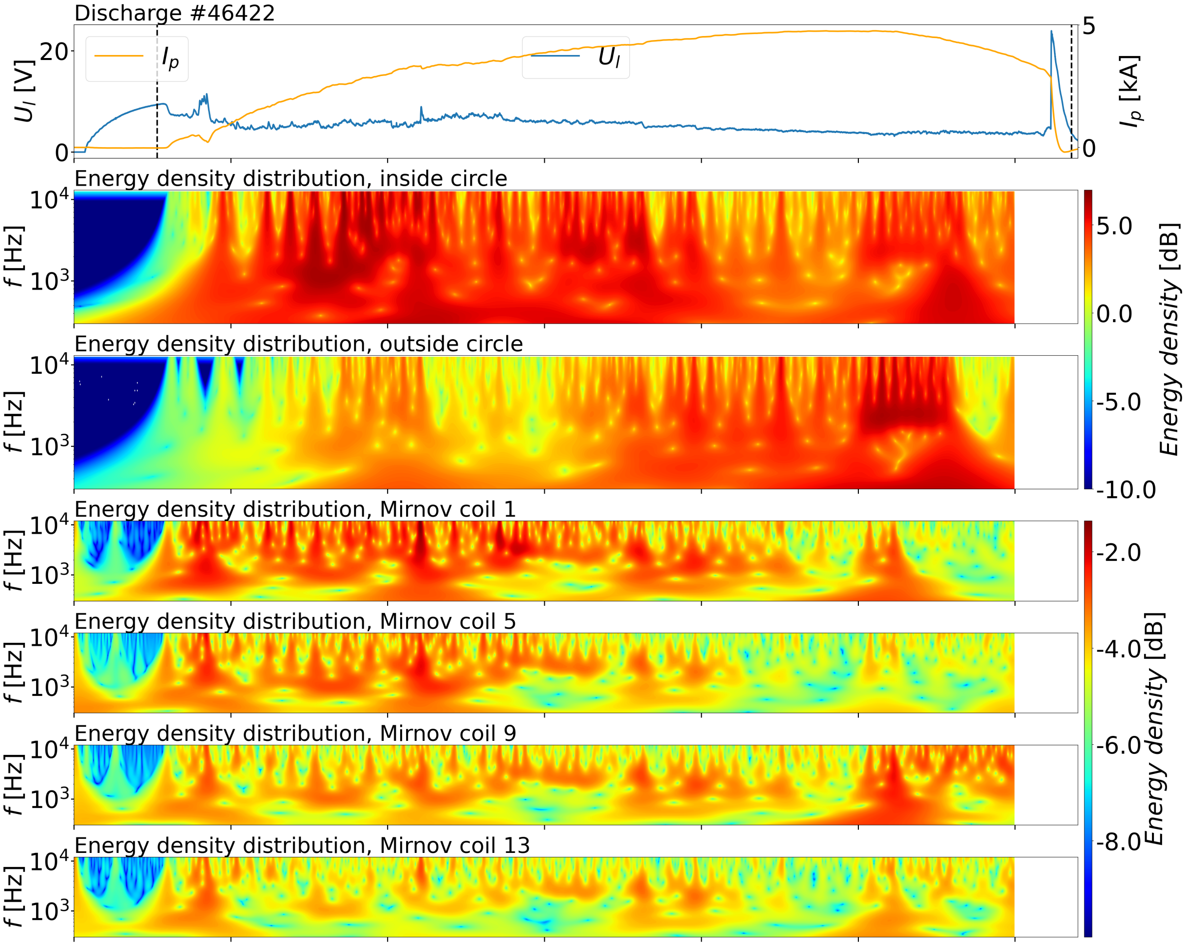

Figure 11: Each signal (Mirnov coils and Timepix3 detector) is analysed via continuous wavelet transform using order-3 analytic Morlet wavelets; the resulting energy densities are shown in lines 2 – 7. U_{loop} and I_p are added for the reference.

precision, while higher-order wavelets yield sharper frequency discrimination with reduced temporal accuracy. The sampling frequency was set to 50 kHz, with a scale resolution of $dj = 1/16$. This sampling frequency is the highest technically possible in this case, since the signal from Mirnov's coils is recorded every 20 μs, which corresponds to a frequency of 50 kHz. The dj parameter controls the logarithmic resolution of the scales in the CWT. In the PyCWT implementation, the scales are defined according to $a_j = s_0 2^{j dj}$, where a_j is the scale at index j, s_0 is the smallest scale, and dj determines the step between successive scales. A smaller value of dj produces finer scale (and therefore frequency) resolution, as more scales are generated within the same frequency band.

In the last two plots in Figure 12, the minimum wavelet coherence of the HXR signals for the Be window area and the rest of the sensor with the signals from the individual Mirnov coils is shown. To detect time-localised correlated oscillations between HXR and magnetic (Mirnov) signals we use wavelet coherence, i.e. the (smoothed) normalized cross-wavelet power localised in the time–frequency plane [48]. For signals

x and y the wavelet coherence is computed as

$$\mathrm{COH}_{x,y}(\mu,\xi)=\frac{\left|\overline{W_x(\mu,\xi)W_y^*(\mu,\xi)}\right|}{\sqrt{\overline{W_x(\mu,\xi)W_x^*(\mu,\xi)}\;\overline{W_y(\mu,\xi)W_y^*(\mu,\xi)}}},\tag{2}$$

where the overbar denotes smoothing (averaging) performed to stabilise the estimates; the role and necessity of such smoothing for analytic wavelets are discussed in [48] and practical implementation choices are described in applied references (e.g. [41]). The wavelet spectra were smoothed by convolution with an affine-invariant rectangular kernel with a smoothing window of width equal to 10 wavelet lengths. Specifically, the wavelet coherence of the HXR signal with the signal from each Mirnov coil is first calculated using formula (2), and then the minimum wavelet coherence is determined from these four datasets.

A comparison of the energy spectra from different time windows shows that the intensity and energy of the detected HXR produced by REs vary over time. During the discharge phase, when the highest-energy HXR is detected (Figure 8), these signals are coherent with those from the magnetic diagnostics (Figure 12).

Minimum wavelet coherence indicates the regions of the time–frequency plane in which the HXR signal is coherent with the MHD signals. This suggests that certain populations of runaway electrons may be modulated by a particular type of MHD activity. To verify this, dominant oscillatory components are identified as coherent ridges in the wavelet minimum coherence map Figure 13). These ridges are trajectories where the wavelet energy concentrates and are related to the instantaneous frequency of modulated components [44]. Ridge theory and practical extraction procedures (local maxima per time slice, linking under continuity constraints, smoothing and segment selection) are treated in [44, 49, 50].

An analysis of a vacuum discharge was also carried out. In this case, wavelet transforms are performed only for the Mirnov coils. No signal was observed on the Timepix3 detector. Furthermore, the coherences between individual coils are calculated, and from the coherences of the individual Mirnov coil pairs, the minimum wavelet coherence and the average wavelet coherence are determined. In the data from the vacuum discharge, no distinct frequency is observed that could affect the results from the plasma discharges. This analysis proved that the magnetic diagnostics do not detect any technical frequencies (e.g. from amplifiers) that could interfere with the analysis of discharges with plasma and that would need to be taken into account. This supports the conclusion that RE losses in plasma discharges may be linked to MHD mode activity in the plasma.

Wavelet coherence as well as cross-wavelets are complex quantities, the argument (phase) of which gives the instantaneous phase difference between two signals [48]. For two signals $x(t)$, $y(t)$, the cross-wavelet spectrum is defined as $W_{xy}(\mu,\xi)=W_x(\mu,\xi)W_y^*(\mu,\xi)$ and the coherence phase as

$$\Delta\varphi(\mu,\xi)=\arg(W_{xy}(\mu,\xi)),\tag{3}$$

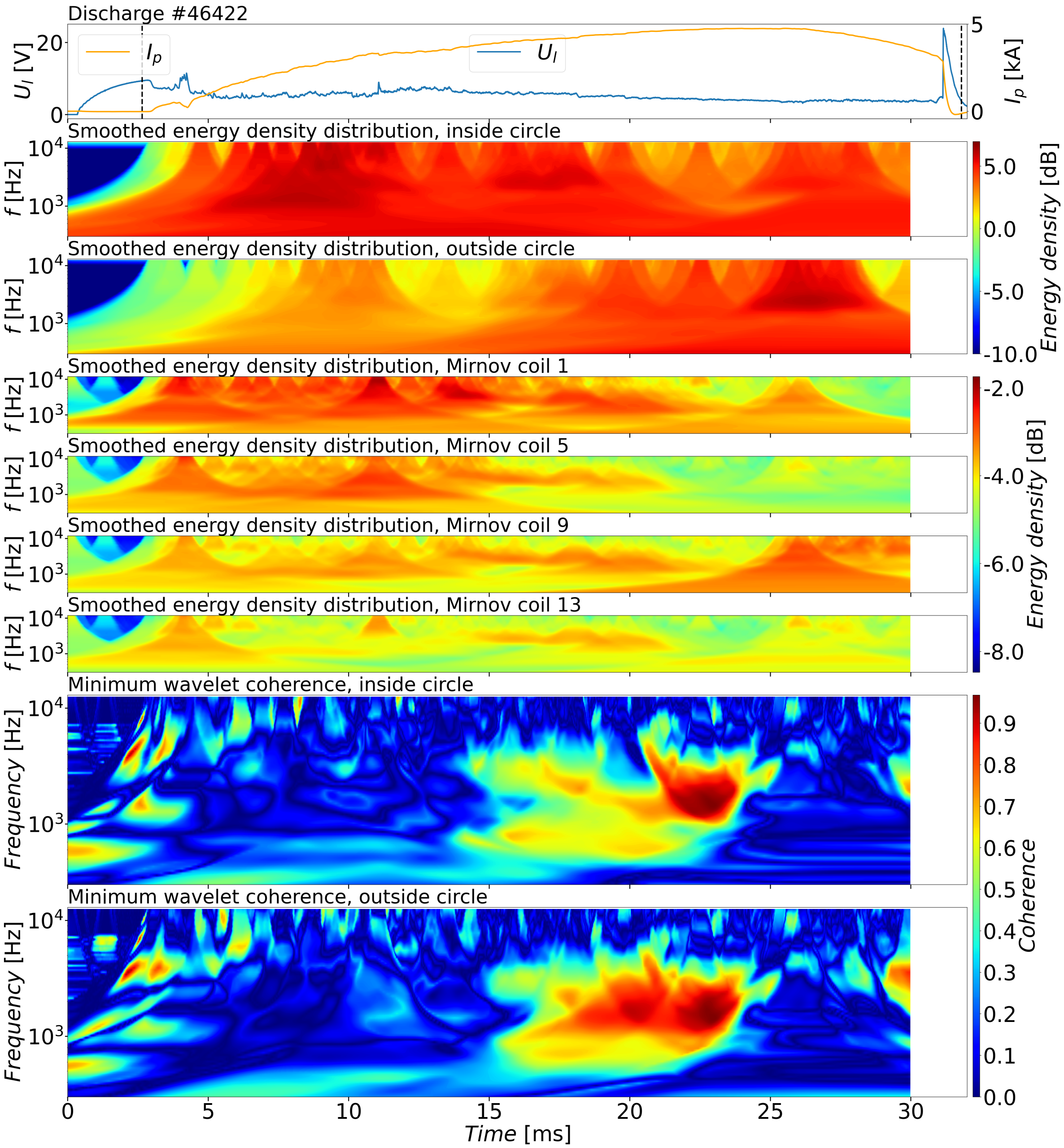

Figure 12: Each signal (Mirnov coils and Timepix3 detector) is analysed via continuous wavelet transform using order-3 analytic Morlet wavelets; the resulting smoothed energy densities are shown in lines $2-7$. The last two lines show the minimum wavelet coherence for each Mirnov coil-Timepix3 signal pair. U_{loop} and I_p are added for the reference.

which is referred to as the wavelet coherence phase [48]. This phase, lying between $-\pi$ and π, corresponds to the relative delay or shift between the signals at a given time and frequency scale.

The cone of influence (COI), i.e. regions adjacent to the signal edges where CWT estimates are affected by boundary effects, is taken into account when interpreting TF (time-frequency) maps and ridge statistics [48].

First, ridges, which are continuous curves of local amplitude maxima, are determined in minimum wavelet coherence images. Ridge analysis tracks these continuous trajectories of maxima in a time sequence. These ridges are shown in Figure 13.

The phase shift is calculated along each ridge using Eq. (3) between each Mirnov coil and the time evolutions of HXR signals from Timepix3 for the two energy regions. In Figure 14, the phase shift for the HXR signal and the high-field-side Mirnov coil is shown. Almost all of the separated ridges exhibit a roughly constant phase shift between 0 and $\pi/2$, with only minor variations among the ridges. There is very little variation between the 4 Mirnov coils located at different locations around the plasma (Figure 4) in this sense. One exception is ridge 1 (Figure 13, upper panel), which was identified in a region of the sensor with a direct line of sight through the beryllium window (inside the red circle). This ridge differs in both the magnitude of the phase shift and its temporal stability, as illustrated in the upper panel of Figure 14, and a trend in the phases across the different Mirnov coils might indicate a well-defined mode structure. Further refinement of the ridge detection algorithm may enable the identification of additional ridges, revealing further differences between data originating from the beryllium window line of sight and that from the remaining sensor area. Such differences could indicate the potential to detect both SXR and HXR using a single device. A more detailed analysis of the correlations between MHD activity and HXR (and possibly SXR) emission, as well as the determination of MHD mode numbers, will be conducted in the future. However, the present results are consistent with the possibility that MHD modes detected by the Mirnov coils may influence runaway electron losses.

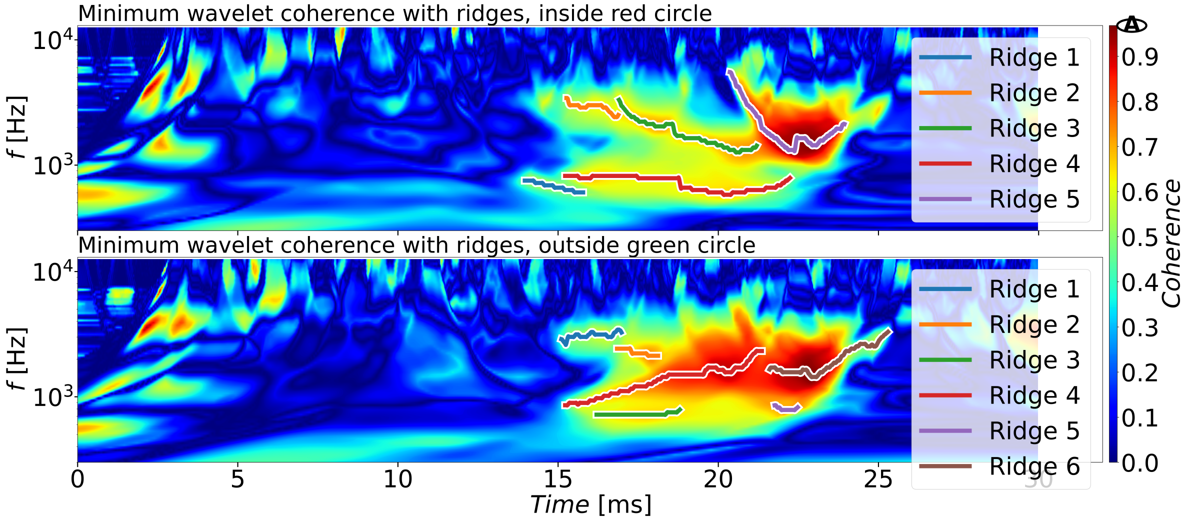

Figure 13: Coherent ridges are identified in the wavelet minimum coherence map.

The paragraph below presents the summary of this chapter. To determine the coherence between the HXR signals from the Timepix3 detector and the Mirnov coils, continuous wavelet transforms were performed and the minimum wavelet coherence was

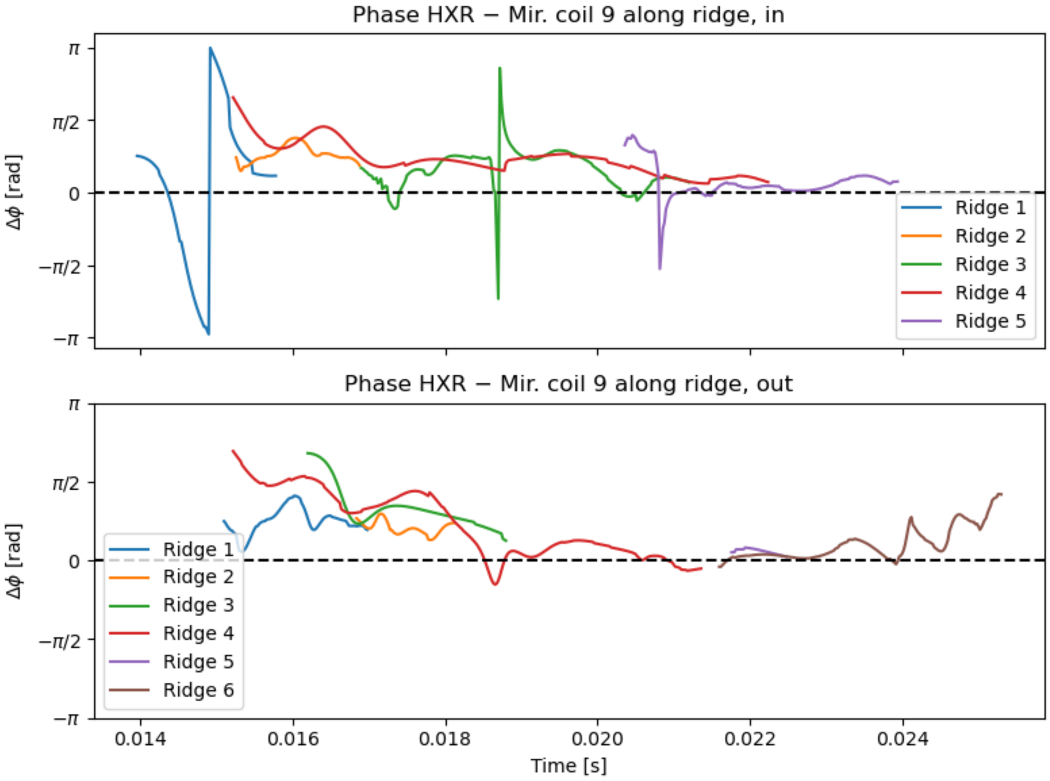

Figure 14: The phase shift for the HXR signal (from inside red circle) and Mirnov coil number 9.

calculated. As can be seen in Figure 12, the results demonstrate the presence of regions of increased coherence between the detector and Mirnov coil signals during the discharge. This may indicate a connection between MHD activity and RE losses. To verify this, coherent ridges are identified (see Figure 13) in the wavelet minimum coherence map. Phase shift calculations along the ridges, shown in Figure 14, indicate a nearly constant phase shift for almost every ridge. The calculation of phase shift along ridges depends on the quality of separation of individual ridges. Ridge separation currently works satisfactorily, but there is room for improvement in the detection algorithm, which will be addressed in future work. A total of 15 plasma discharges were analyzed, of which 12 exhibited the same phenomena as those described in this work.

A comparison of regions with high minimum wavelet coherence, followed by an increase in HXR detection on the Timepix3 detector, suggests that the MHD modes detected by the Mirnov coils may modulate RE losses. The maxima of coherence and the corresponding phase shifts correlate with moments of an increased number and energy of detected HXR (see Figure 12 and Figure 8).

4. Conclusion

In this study, we employed a methodology that combined the AdvaPix Timepix3 pixel detector with continuous wavelet transform, as well as the quantification of wavelet coherence in relation to magnetic signals from the Mirnov coils on the GOLEM tokamak. This time–frequency analysis identified regions of increased coherence between HXR signals from the Timepix3 detector and Mirnov coil signals. This indicates that runaway electron losses in these intervals may be modulated by MHD modes. Furthermore, we demonstrated that comparing energy spectra from different time windows reveals differences in the energies and numbers of RE losses.

Phase shifts observed along certain time–frequency ridges are consistent across multiple discharges, suggesting that populations of REs may be modulated by MHD activity. Analysis of vacuum discharges showed that the identified frequency structures are not artefacts of the behaviour of the laboratory equipment used on the tokamak, but are associated with the presence of plasma and its MHD activity. Thus, the study confirms the practical applicability of Timepix3 for diagnosing correlations between MHD modes and runaway electrons.

Future work could focus on determining the toroidal and poloidal mode numbers and comparing the results with those from other diagnostics. Overall, this combination of detection and time–frequency analysis paves the way for linking MHD mode parameters with RE losses, which is significant for both further research and the design of strategies to mitigate the harmful effects of runaway electrons.

5. Acknowledgement

This work was supported by the Grant Agency of the Czech Technical University in Prague, grant No. SGS24/144/OHK4/3T/14 and SGS25/160/OHK4/3T/14. This work has been carried out within the framework of the EUROfusion Consortium, funded by the European Union via the Euratom Research and Training Programme (Grant Agreement No 101052200 - EUROfusion). Views and opinions expressed are however those of the author(s) only and do not necessarily reflect those of the European Union or the European Commission. Neither the European Union nor the European Commission can be held responsible for them.

References

[1] DREICER, H., 1960. Electron and Ion Runaway in a Fully Ionized Gas. II. Online. *Physical Review*. 1960-1-15, roč. 117, č. 2, pp. 329-342. ISSN 0031-899X. Available at: `https://doi.org/10.1103/physrev.117.329` . [accessed 2025-12-10].

[2] RICCARDO, V; ARNOUX, G; CAHYNA, P; HENDER, T C; HUBER, A et al., 2010. JET disruption studies in support of ITER. Online. *Plasma Physics and Controlled Fusion*. 2010-11-15, roč. 52, č. 12, p. 124018. ISSN 0741-3335. Available at: `https://doi.org/10.1088/0741-3335/52/12/124018` . [accessed 2025-12-10].

[3] MLYNAR, J; FICKER, O; MACUSOVA, E; MARKOVIC, T; NAYDENKOVA, D et al., 2018. Runaway electron experiments at COMPASS in support of the EUROfusion ITER physics research. Online. *Plasma Physics and Controlled Fusion*. 2018-11-13, roč. 61, č. 1, p. 014010. ISSN 0741-3335. Available at: `https://doi.org/10.1088/1361-6587/aae04a` . [accessed 2025-12-10].

[4] PLYUSNIN, V.V.; KIPTILY, V.G.; SHEVELEV, A.E.; KHILKEVITCH, E.M.; GERASIMOV, S. et al., 2019. Hard X-ray Bremsstrahlung of relativistic Runaway Electrons in JET. Online. *Journal of Instrumentation*. 2019-9-23, roč. 14, č. 09, pp. C09042-C09042. ISSN 1748-0221. Available at: `https://doi.org/10.1088/1748-0221/14/09/c09042` . [accessed 2025-12-17].

[5] FICKER, O.; MLYNAR, J.; VLAINIC, M.; CEROVSKY, J.; URBAN, J. et al., 2017. Losses of runaway electrons in MHD-active plasmas of the COMPASS tokamak. Online. *Nuclear Fusion*. 2017-5-11, roč. 57, č. 7, p. 076002. ISSN 0029-5515. Available at: `https://doi.org/10.1088/1741-4326/aa6aba` . [accessed 2025-12-09].

[6] MLYNAR, J.; FICKER, O.; VLAINIC, M.; WEINZETTL, W. and IMRISEK, M., 2015. Effects of Plasma Control on Runaway Electrons in the COMPASS Tokamak. Online. In: *42nd EPS Conference on Plasma Physics (EPS 2015)*. Lisbon, Portugal: European Physical Society (EPS), p. 933-936. ISBN 9781510829466. Available at: `https://info.fusion.ciemat.es/OCS/eps2015pap/pdf/P4.102.pdf` . [accessed 2025-12-09].

[7] PAPROK, R.; KRLIN, L. and STOCKEL, J., 2013. Observation and Prediction of Runaway Electrons in the COMPASS Tokamak. Online. In: *WDS'13 Proceedings of Contributed Papers*. Prague: MATFYZPRESS, p. 60-66. ISBN 978-80-7378-251-1. Available at: `https://physics.mff.cuni.cz/wds/proc/pdf13/WDS13_209_f2_Paprok.pdf` . [accessed 2025-12-09].

[8] VLAINIĆ, Miloš; MLYNÁŘ, Jan; WEINZETTL, Vladímir; PAPŘOK, Richard; IMRÍŠEK, Martin et al., 2015. First dedicated observations of runaway electrons in the COMPASS tokamak. Online. *Nukleonika*. 2015-6-1, roč. 60, č. 2, pp. 249-255. ISSN 0029-5922. Available at: `https://doi.org/10.1515/nuka-2015-0052` . [accessed 2025-12-09].

[9] OGURA, K.; TANAKA, H.; IDE, S.; IIDA, M.; HANADA, K. et al., 1991. Study of the fast electron distribution function in lower hybrid and electron cyclotron current driven plasmas in the WT-3 tokamak. Online. *Nuclear Fusion*. 1991-6-1, roč. 31, č. 6, pp. 1015-1033. ISSN 0029-5515. Available at: `https://doi.org/10.1088/0029-5515/31/6/002` . [accessed 2025-12-08].

[10] SHEVELEV, A; KHILKEVITCH, E; TUKACHINSKY, A; PANDYA, S; ASKINAZI, L et al., 2018. Study of runaway electrons in TUMAN-3M tokamak plasmas. Online. *Plasma Physics and Controlled Fusion*. 2018-5-24, roč. 60, č. 7, p. 075009. ISSN 0741-3335. Available at: `https://doi.org/10.1088/1361-6587/aac0d5` . [accessed 2025-12-08].

[11] MA, T.K.; CHEN, Z.Y.; HUANG, D.W.; TONG, R.H.; YAN, W. et al., 2017. Development of hard X-ray spectrometer with high time resolution on the J-TEXT tokamak. Online. *Nuclear Instruments and Methods in Physics Research Section A: Accelerators, Spectrometers, Detectors and Associated Equipment*. Č. 856, pp. 81-85. ISSN 0168-9002. Available at: `https://doi.org/10.1016/j.nima.2017.02.089` . [accessed 2025-12-08].

[12] ZHANG, Y. P.; MAZON, D.; PEYSSON, Y.; MALARD, P.; ZHANG, P. F. et al., 2019. Measurements of the fast electron bremsstrahlung during lower hybrid current drive in the HL-2A tokamak. Online. *AIP Advances*. 2019-8-1, roč. 9, č. 8. ISSN 2158-3226. Available at: `https://doi.org/10.1063/1.5110233` . [accessed 2025-12-08].

[13] CHEN, Z.Y.; WAN, B.N.; LIN, S.Y.; SHI, Y.J.; HU, L.Q. et al., 2006. Measurement of the non-thermal bremsstrahlung emission between 20 and 7000 keV in the HT-7 Tokamak. Online. *Nuclear Instruments and Methods in Physics Research Section A: Accelerators, Spectrometers, Detectors and Associated Equipment*. Roč. 560, č. 2, pp. 558-563. ISSN 0168-9002. Available at: `https://doi.org/10.1016/j.nima.2005.12.200` . [accessed 2025-12-08].

[14] CHEN, Z. Y.; WAN, B. N.; LIN, S. Y.; SHI, Y. J.; HU, L. Q. et al., 2006. Measurement of the runaway electrons in the HT-7 tokamak. Online. *Review of Scientific Instruments*. 2006-1-1, roč. 77, č. 1. ISSN 0034-6748. Available at: `https://doi.org/10.1063/1.2140488` . [accessed

2025-12-08].

[15] SIMONS, L.; CEROVSKY, J.; DECKER, J.; DUVAL, B. P.; FICKER, O. et al., 2025. A lanthanum bromide detector of runaway electrons for TCV. Online. *Review of Scientific Instruments*. 2025-9-1, roč. 96, č. 9. ISSN 0034-6748. Available at: `https://doi.org/10.1063/5.0277312` . [accessed 2025-12-09].

[16] DAL MOLIN, A; NOCENTE, M; DALLA ROSA, M; PANONTIN, E; RIGAMONTI, D et al., 2023. A new hard x-ray spectrometer for runaway electron measurements in tokamaks. Online. *Measurement Science and Technology*. 2023-5-23, roč. 34, č. 8, p. 085501. ISSN 0957-0233. Available at: `https://doi.org/10.1088/1361-6501/acd46c` . [accessed 2025-12-09].

[17] SHEVELEV, A.; KHILKEVITCH, E.; ILIASOVA, M.; NOCENTE, M.; PAUTASSO, G. et al., 2021. Study of runaway electron dynamics at the ASDEX Upgrade tokamak during impurity injection using fast hard x-ray spectrometry. Online. *Nuclear Fusion*. 2021-9-30, roč. 61, č. 11, p. 116024. ISSN 0029-5515. Available at: `https://doi.org/10.1088/1741-4326/ac2638` . [accessed 2025-12-09].

[18] SHEVELEV, A.E.; KHILKEVITCH, E.M.; LASHKUL, S.I.; ROZHDESTVENSKY, V.V.; ALTUKHOV, A.B. et al., 2016. High performance gamma-ray spectrometer for runaway electron studies on the FT-2 tokamak. Online. *Nuclear Instruments and Methods in Physics Research Section A: Accelerators, Spectrometers, Detectors and Associated Equipment*. Č. vol. 830, pp. 102-108. ISSN 0168-9002. Available at: `https://doi.org/10.1016/j.nima.2016.05.075` . [accessed 2025-12-09].

[19] SHEVELEV, A.E.; KHILKEVITCH, E.M.; LASHKUL, S.I.; ROZHDESTVENSKY, V.V.; PANDYA, S.P. et al., 2017. Runaway electron studies with hard x-ray and microwave diagnostics in the FT-2 lower hybrid current drive discharges. Online. *Nuclear Fusion*. 2017-11-23, roč. 58, č. 1, p. 016034. ISSN 0029-5515. Available at: `https://doi.org/10.1088/1741-4326/aa8cea` . [accessed 2025-12-09].

[20] BIZARRO, João P.; PEYSSON, Yves; BONOLI, Paul T.; CARRASCO, Joël; DE WIT, Thierry Dudok et al., 1993. On self-consistent ray-tracing and Fokker—Planck modeling of the hard x-ray emission during lower-hybrid current drive in tokamaks. Online. *Physics of Fluids B: Plasma Physics*. 1993-9-1, roč. 5, č. 9, pp. 3276-3283. ISSN 0899-8221. Available at: `https://doi.org/10.1063/1.860664` . [accessed 2025-12-09].

[21] ZHU, X.; ZENG, L.; LIANG, Y.; LIN, S.; LIU, Y. et al., 2020. Observation of two threshold fields for runaway-electron generation in tokamaks. Online. *Nuclear Fusion*. 2020-7-2, roč. 60, č. 8, p. 084002. ISSN 0029-5515. Available at: `https://doi.org/10.1088/1741-4326/ab96f3` . [accessed 2025-12-09].

[22] ZHANG, Y. P.; LIU, Yi; SONG, X. Y.; YUAN, G. L.; CHEN, W. et al., 2010. Measurements of the fast electron bremsstrahlung emission during electron cyclotron resonance heating in the HL-2A tokamak. Online. *Review of Scientific Instruments*. 2010-10-1, roč. 81, č. 10. ISSN 0034-6748. Available at: `https://doi.org/10.1063/1.3488966` . [accessed 2025-12-09].

[23] PEYSSON, Yves and IMBEAUX, Frédéric, 1999. Tomography of the fast electron bremsstrahlung emission during lower hybrid current drive on TORE SUPRA. Online. *Review of Scientific Instruments*. 1999-10-1, roč. 70, č. 10, pp. 3987-4007. ISSN 0034-6748. Available at: `https://doi.org/10.1063/1.1150025` . [accessed 2025-12-09].

[24] GNESIN, S.; CODA, S.; DECKER, J. and PEYSSON, Y., 2008. Suprathermal electron studies in the TCV tokamak: Design of a tomographic hard-x-ray spectrometer. Online. *Review of Scientific Instruments*. 2008-10-1, roč. 79, č. 10. ISSN 0034-6748. Available at: `https://doi.org/10.1063/1.2957843` . [accessed 2025-12-09].

[25] PEYSSON, Y.; CODA, S. and IMBEAUX, F., 2001. Hard X-ray CdTe tomography of tokamak fusion plasmas. Online. *Nuclear Instruments and Methods in Physics Research Section A: Accelerators, Spectrometers, Detectors and Associated Equipment*. Roč. 458, č. 1-2, pp. 269-274. ISSN 0168-9002. Available at: `https://doi.org/10.1016/s0168-9002(00)00870-6` . [accessed 2025-12-09].

[26] CHENG, S. K.; ZHU, Y. B.; CHEN, Z. Y.; LI, Y. X.; BAI, R. H. et al., 2021. Tangential hard x-ray diagnostic array on the EXL-50 spherical tokamak. Online. *Review of Scientific Instruments.* 2021-4-1, roč. 92, č. 4. ISSN 0034-6748. Available at: `https://doi.org/10.1063/5.0040636` . [accessed 2025-12-09].

[27] LIPTAC, J.; PARKER, R.; TANG, V.; PEYSSON, Y. and DECKER, J., 2006. Hard x-ray diagnostic for lower hybrid experiments on Alcator C-Mod. Online. *Review of Scientific Instruments.* 2006-10-1, roč. 77, č. 10. ISSN 0034-6748. Available at: `https://doi.org/10.1063/1.2214695` . [accessed 2025-12-09].

[28] CEROVSKY, J.; FICKER, O.; SVOBODA, V.; MACUSOVA, E.; MLYNAR, J. et al., 2022. Progress in HXR diagnostics at GOLEM and COMPASS tokamaks. Online. *Journal of Instrumentation.* 2022-1-1, roč. 17, č. 01, p. C01033. ISSN 1748-0221. Available at: `https://doi.org/10.1088/1748-0221/17/01/c01033` . [accessed 2025-12-09].

[29] SVIHRA, Peter; BREN, David; CASOLARI, Andrea; CEROVSKY, Jaroslav; DHYANI, Pravesh et al., 2019. Runaway electrons diagnostics using segmented semiconductor detectors. Online. *Fusion Engineering and Design.* Roč. 146, Part A, pp. 316-319. ISSN 0920-3796. Available at: `https://doi.org/10.1016/j.fusengdes.2018.12.054` . [accessed 2025-09-07].

[30] NOVOTNY, L.; CEROVSKY, J.; DHYANI, P.; FICKER, O.; HAVRANEK, M. et al., 2020. Runaway electron diagnostics using silicon strip detector. Online. *Journal of Instrumentation.* 2020-7-10, roč. 15, č. 07, pp. C07015-C07015. ISSN 1748-0221. Available at: `https://doi.org/10.1088/1748-0221/15/07/c07015` . [accessed 2025-12-09].

[31] POIKELA, T; PLOSILA, J; WESTERLUND, T; CAMPBELL, M; GASPARI, M De et al., 2014. Timepix3: a 65K channel hybrid pixel readout chip with simultaneous ToA/ToT and sparse readout. Online. *Journal of Instrumentation.* 2014-5-13, roč. 9, č. 05, pp. C05013-C05013. ISSN 1748-0221. Available at: `https://doi.org/10.1088/1748-0221/9/05/c05013` . [accessed 2025-09-04].

[32] LINHART, Vladimir; BREN, David; CASOLARI, Andrea; CEROVSKY, Jaroslav; FARNIK, Michal et al., 2018. First Measurement of X-rays Generated by Runaway Electrons in Tokamaks Using a TimePix3 Device with 1 mm thick Silicon Sensor. Online. *2018 IEEE Nuclear Science Symposium and Medical Imaging Conference Proceedings (NSS/MIC).* Pp. 1-9. Available at: `https://doi.org/10.1109/nssmic.2018.8824534` . [accessed 2025-09-07].

[33] MALEC, Stepan; LINHART, Vladimir and SVOBODA, Vojtech, 2021. Correlations in Signals Generated by Runaway Electrons in the GOLEM Tokamak measured using the Timepix3 Detection Modules. Online. *2021 IEEE Nuclear Science Symposium and Medical Imaging Conference (NSS/MIC).* 2021-10-16, pp. 1-6. Available at: `https://doi.org/10.1109/nss/mic44867.2021.9875920` . [accessed 2025-09-07].

[34] KULKOV, S.; MARCISOVSKY, M.; SVIHRA, P.; TUNKL, M.; VAN BEUZEKOM, M. et al., 2022. Detection of runaway electrons at the COMPASS tokamak using a Timepix3-based semiconductor detector. Online. *Journal of Instrumentation.* 2022-2-1, roč. 17, č. 02, p. P02030. ISSN 1748-0221. Available at: `https://doi.org/10.1088/1748-0221/17/02/p02030` . [accessed 2025-09-07].

[35] SVOBODA, V.; HUANG, B.; MLYNÁŘ, J.; POKOL, G.I.; STÖCKEL, J. et al., 2011. Multi-mode remote participation on the GOLEM tokamak. Online. *Fusion Engineering and Design.* Roč. 86, č. 6-8, pp. 1310-1314. ISSN 0920-3796. Available at: `https://doi.org/10.1016/j.fusengdes.2011.02.069` . [accessed 2025-09-07].

[36] *Tokamak GOLEM wiki.* Online. Available at: `http://golem.fjfi.cvut.cz/wiki/`. [accessed 2025-09-07].

[37] APXT3M-Xxx200128-AdvaPIX-TPX3-Datasheet-2020-05-26. *Lasphotonics* [online]. 2020 [cit. 2023-01-02]. Dostupné z: https://lasphotonics.com/wp-content/uploads/2020/10/APXT3M-Xxx200128-AdvaPIX-TPX3-Datasheet-2020-05-26.pdf

[38] Thompson, C.A., Kirz, J., Attwood, T.D., Gullikson, M.E., Liu, Y., et al. (2009) X-Ray Data Booklet. 3rd Edition, Lawrence Berkeley National Laboratory, Berkeley, CA. `https:`

`//xdb.lbl.gov/` . [accessed 2025-12-17]

[39] HELLER, M. V. A. P.; BRASILIO, Z. A.; CALDAS, I. L.; STÖCKEL, J. and PETRZILKA, J., 1999. Scrape-off layer intermittency in the Castor tokamak. Online. *Physics of Plasmas.* 1999-3-1, roč. 6, č. 3, pp. 846-853. ISSN 1070-664X. Available at: `https://doi.org/10.1063/1.873324` . [accessed 2025-09-07].

[40] PAPP, G; POKOL, G I; POR, G; MAGYARKUTI, A; LAZÁNYI, N et al., 2011. Low frequency sawtooth precursor activity in ASDEX Upgrade. Online. *Plasma Physics and Controlled Fusion.* 2011-4-7, roč. 53, č. 6, p. 065007. ISSN 0741-3335. Available at: `https://doi.org/10.1088/0741-3335/53/6/065007` . [accessed 2025-12-17].

[41] POKOL, Gergo; LAZANYIL, N.; POR, Gabor; MAGYARKUTI, András; PAPP, Gergely et al., 2010. A wavelet based method for detecting transient plasma waves and determining their spatial structure. Online. *37th European Physical Society Conference on Plasma Physics, Contributed Papers.* Roč. 37. Available at: `https://www.researchgate.net/publication/47820550_A_wavelet_based_method_for_detecting_transient_plasma_waves_and_determining_their_spatial_structure` . [accessed 2025-09-07].

[42] CASOLARI, A.; GOBBIN, M.; SPIZZO, G.; CEROVSKY, J.; FICKER, O. et al., 2023. Subdiffusive transport of runaway electrons in presence of small amplitude MHD perturbations in COMPASS. Online. *Nuclear Fusion.* 2023-12-1, roč. 64, č. 1, p. 016027. ISSN 0029-5515. Available at: `https://doi.org/10.1088/1741-4326/ad0e31` . [accessed 2025-09-08].

[43] GHANBARI, K.; GHORANNEVISS, M.; ELAHI, A. Salar and SAVIZ, S., 2014. X-ray irradiation analysis based on wavelet transform in tokamak plasma. Online. *Journal of X-Ray Science and Technology.* Roč. 22, č. 6, pp. 777-783. ISSN 0895-3996. Available at: `https://doi.org/10.3233/xst-140462` . [accessed 2025-12-17].

[44] MALLAT, S. G., c2009. *A wavelet tour of signal processing: the sparse way.* Online. 3rd ed. Amsterdam: Elsevier/Academic Press. ISBN 978-0-12-374370-1. Available at: `https://doi.org/10.1016/B978-0-12-374370-1.X0001-8` . [accessed 2025-09-07].

[45] XIAO, C and ET AL., 2008. Investigations of Magnetohydrodynamic Instabilities in the STOR-M tokamak. Online. In: *22nd IAEA Fusion Energy Conference.* [accessed 2025-09-04].

[46] GROSSMANN, A. and MORLET, J., 1984. Decomposition of Hardy Functions into Square Integrable Wavelets of Constant Shape. Online. *SIAM Journal on Mathematical Analysis.* Roč. 15, č. 4, pp. 126-139. Available at: `https://doi.org/https://doi.org/10.1137/0515056` . [accessed 2025-09-07].

[47] GOUPILLAUD, P.; GROSSMANN, A. and MORLET, J., 1984. Cycle-octave and related transforms in seismic signal analysis. Online. *Geoexploration.* Roč. 23, č. 1, pp. 85-102. Available at: `https://doi.org/https://doi.org/10.1016/0016-7142(84)90025-5` . [accessed 2025-09-07].

[48] TORRENCE, Christopher and P. COMPO, Gilbert, 1998. A Practical Guide to Wavelet Analysis. Online. *Bulletin of the American Meteorological Society.* Roč. 79, č. 1, pp. 61—78. Available at: https://doi.org/10.1175/1520-0477(1998)079 ¡0061:APGTWA¿2.0.CO;2. [accessed 2025-09-07].

[49] CARMONA, Rene; HWANG, Wen-Liang and TORRESANI, Bruno, 1998. *Practical Time-Frequency Analysis.* Online. Academic Press. ISBN 9780080539423. Available at: `https://doi.org/10.1016/S1874-608X(98)80025-3` . [accessed 2025-09-07].

[50] First- and Higher-Order Correlation Detection Using Wavelet Transforms, FEBRUARY 2003. Online. *Journal of Engineering Mechanics.* Roč. 129, č. 2, pp. 188-201. Available at: `https://doi.org/10.1061/~ASCE!0733-9399~2003!129:2~188!` . [accessed 2025-09-04].

[51] http://golem.fjfi.cvut.cz/shots/46422/